## PAPER

# Effect of $Ti_{1-x}Fe_xO_2$ photoanodes on the performance of dye-sensitized solar cells utilizing natural *betalain pigments* extracted from *Beta vulgaris* (*BV*)

Abhishek Srivastava, [ID][a] Jena Akash Kumar Satrughna, [ID][b] Manish Kumar Tiwari, [ID][a] Archana Kanwade, [ID][a] Subhash Chand Yadav, [ID][a] Kiran Bala[c] and Parasharam M. Shirage*[a]

In order to enhance the performance and stability of the naturally occurring dye-based DSSCs, various engineered photoanodes were employed. In this study, Fe-doped $TiO_2$ nanorod (NR) based photoanodes were synthesized on transparent conducting fluorine doped tin oxide (FTO) electrodes with the different concentrations of Fe ($Ti_{1-x}Fe_xO_2$, $x = 0-0.1$) by a simple and economical hydrothermal method. The impact of Fe doping on the physicochemical and electrical characteristics of $Ti_{1-x}Fe_xO_2$ photoanodes was investigated. The effect of $Ti_{1-x}Fe_xO_2$ photoanodes in a dye-sensitized solar cell (DSSC) setup utilizing a natural dye extracted from *Beta vulgaris* (*BV*) was analyzed. The photovoltaic performance of the fabricated device using $Ti_{1-x}Fe_xO_2$ NRs is tested by current density–voltage (*J–V*) and incident photon-to-electron conversion efficiency (IPCE) characteristics to estimate the power conversion efficiency (PCE). The maximum photocurrent density of the DSSC device increased from 80 to 129.758 $\mu A\ cm^{-2}$, whereas the PCE enhanced nearly twice from 0.26% to 0.52% with the insertion of 5 at% Fe in $TiO_2$ NRs. The experimental result demonstrates that the charge injection and separation are significantly improved by the $Ti_{1-x}Fe_xO_2$ interlayer. We predict that $Ti_{1-x}Fe_xO_2$ photoanodes with improved responsiveness can replace the pure $TiO_2$ nanostructures for promising photovoltaic applications. In addition to photovoltaics, these $Ti_{1-x}Fe_xO_2$ photoanodes may serve as an encouraging approach for photocatalysis and photo sensors.

## 1. Introduction

In 1991, the first DSSC was developed by O'Regan and Gratzel at UC Berkeley and since then intensive investigations have been made to improve the device's performance.[1] It also grabs the attention of researchers because of its low production cost and very low environmental and health impact. Production of DSSCs is very fast, easy, and economical as compared to other emerging and conventional photovoltaics, while its performance crossed over 14%.[2] Moreover, DSSCs based on natural dyes such as extracts of leaves, flowers, and fruit peels, are also attracting researchers' attention. However, the performance of such DSSCs is directly influenced by the charge collection

efficiency, photo-scattering ability, and recombination rates.[3,4] Apart from this, the effective operation of natural dye-based DSSCs is still under investigation and is lower than that of conventional photovoltaic technology such as silicon solar cells, which hinders their wide applications. To achieve better and high PCE, the design of photoanodes having optimum dye loading, better sunlight scattering, effective transportation of charge carriers, and reduced charge carrier recombination is the most crucial thing to look into.[5] In general, metal oxides are preferred for the photoanodes and mesoporous nanostructures of $TiO_2$, $ZnO$, $SnO_2$, $Nb_2O_5$, *etc.*, are widely investigated.[6–8] In all metal oxide-based photoanodes, $TiO_2$ gained the most popularity because of its high surface area, higher chemical stability, less toxicity, significantly high catalyst band edge, very low charge recombination, *etc.*[9] The efficiency of the DSSC depends heavily on the transport and charge separation processes that take place inside the photoanode and, correspondingly, at the photoanode/electrolyte interface, which is substantially morphology and structure-dependent. In contrast, due to large surface site availability in the mesoporous structures, the

[a] *Department of Metallurgy Engineering and Materials Science, Indian Institute of Technology, Indore, 453552, India. E-mail: pmshirage@iiti.ac.in, paras.shirage@gmail.com*

[b] *Department of Physics, Indian Institute of Technology, Indore, 453552, India*

[c] *Department of Biosciences & Biomedical Engineering, Indian Institute of Technology, Indore, 453552, India*

recombination rate shoots up.[10] To overcome this, 1D nano-structures such as nanowires,[11] nanorods,[12] and nanotubes[13] have been explored for photoanodes, which effectively shortened the charge transport path. Previous studies suggested that transition metal doping alters the electronic dimensions, provides structural stability, and tunes the light absorption.[14–17]

In most of the previously reported works on the BV dye-based DSSCs, generally photoanode structures were examined to investigate the device performance and stability. Although many nanostructured photoanodes were investigated it was impossible to significantly enhance the DSSC performance due to the insufficient charge collection efficiency, low photo-scattering, and higher interfacial charge recombination. Therefore, in addition to the dimension of the nanostructures, doping is an interesting trend to tune the absorption edge in the visible spectrum for better photo-charge scattering and collection along with reduced recombination rates. Here this tuning of the absorption edge is driven by the transition of charge carriers in between the d electrons of the doped transition metal ($Fe^{3+}$) and the $TiO_2$ NRs.[18] A new electron state is created within the $TiO_2$ electronic structure due to Fe doping and this will help in reducing the charge recombination *via* capturing photo generated electrons in the valence band of $TiO_2$.[19,20] Fe(III) doping in $TiO_2$ photoanodes is an attractive perspective since (i) $Fe^{3+}$ doping will empower the $TiO_2$ crystal structure and comfortably accommodate within the $TiO_2$ lattice because of their nearly similar ionic radii,[21] (ii) $Fe^{3+}$ doped $TiO_2$ will also assist the improved interfacial charge transportation mediated by shallow charge trapping sites originating deep inside and on the surface of the grown nanostructures as well,[22,23] (iii) $Fe^{3+}$ doping will also allow for photonic excitation with a low energy level because of new energy state formation in the $TiO_2$ bandgap,[24] and (iv) surface adsorption is also improved by $Fe^{3+}$ doping, which gives rise to surface hydroxyl groups and $OH^-$ radicals, which is ascribed to the extra oxygen vacancies within the lattice and on the surface.[25]

In general, the VBs of $TiO_2$ are composed of hybrid O(2p) and Ti(3d) orbitals, while CBs consist of Ti(3d) orbitals, and transition metal doping will significantly alter the electronic and optical properties. Metal ion dopants can change $TiO_2$ electron transport characteristics, enhancing the separation of photo generated charge carriers and shifting the absorption edge of the material to the visible spectrum. Because the dopant energy level lies deep inside the CB of $TiO_2$, more carriers were moving to the surface which can be acting as electron or hole entrapment centers. The absorption spectra of $TiO_2$ shift to higher wavelength as a result of the transition metal doping, which alters the material's electrical energy levels and shrinks the energy band gap.[26]

Fig. 1(a) illustrates the typical charge transport reactions involved in Fe-doped $TiO_2$ photoanodes for DSSC applications. In addition, $Fe^{3+}$ ions in $TiO_2$ can serve as electron and hole trapping centers to prevent electron–hole pair recombination and to increase the production of reactive oxygen species. This leads to the absorption redshift and therefore enhances photo-voltaic activity. When the doping concentration is raised to 5 mM, the bandgap decreases for two important reasons. The first is the doping of $TiO_2$ with $Fe^{3+}$, which produces surface states and oxygen-vacancy sites. The second aspect is the crystallization of haematite $Fe_2O_3$, whose particles have a narrower energy band gap as compared to $TiO_2$, and reducing the bandgap by forming a heterojunction between $Fe_2O_3$ and $TiO_2$.[27] This will further increase visible light absorption. According to the mechanistic theory, produced electrons following light absorption are confined in the $Ti^{3+}$ state below the conduction band minimum, which makes it easier to separate the charges using the heterojunction. With the synthesis of $Ti–O_2^-$ and its subsequent binding as peroxide, those trapped electrons are relocated to $O_2$ species. During the chemical pathway, surface $Fe^{3+}$ sites contribute to the stability of –OH through hydrogen bonding. Even at higher Fe concentrations, the crystal structure of $Ti_{1-x}Fe_xO_2$ is not dramatically affected, but the local structure around the Fe atoms can be severely deformed, particularly when oxygen vacancies are present.[28]

Fig. 1(b) represents three distinguished Fe dopant models to explain the $Fe^{2+, 3+, and 4+}$ occupation in the rutile $TiO_2$ lattice. It is found from the literature that the configuration of $Fe^{3+}$ is the most stable energy structure in which two adjacent Ti-atoms are replaced by Fe and will create an O-vacancy in between. Due to this reason, Fe doping midgap states are introduced and the band gap is drastically reduced. In all the possible arrangements of the Fe dopants, the most stable structure prefers an antiferromagnetic ordering. Also, the haematite and rutile hybrid crystal for Fe–$TiO_2$ formation is energetically not favoured for all modes explained here. Only, we can say that the production of the pure metal oxide spontaneously in an oxygen environment is very challenging. Although, it is difficult to predict whether these phases could be synthesized or not.[29]

Li *et al.* demonstrated the detailed atomistic investigation and concluded that for $Fe^{4+}$ doping, the formation energy was 1.23 eV per Fe-atom, which further lowered with the increase in the Fe concentration. One O-atom acts as a bridge between two Fe dopants in the lowest energy form. With the lowest formation energy of approximately 3 eV per Fe, the integration of $Fe^{2+}$ into the $TiO_2$ matrix is even less stable. In this case, Fe prefers to be integrated into the $TiO_2$ crystal lattice adjacent to the O vacancy. The most likely Ti substituent in the rutile phase is $Fe^{3+}$, with a formation energy of roughly 1 eV per Fe-atom. Similar to $Fe^{2+}$, the lowest-energy arrangement in this instance has two nearest neighbours which are Fe substituents that are situated close to the O-vacancy.[30]

The lattice angles are essentially unaltered in either situation. However, the neighbourhood architecture near the Fe dopants might change considerably. The most noticeable structural modification is the expansion of the Fe–O–Ti or Fe–O–Fe bond angle ($\delta$), which is a frequent outcome when an O vacancy is present. $B^2$ and $B^5$ (apex) Ti–O bond lengths vary from $B^1$, $B^3$, $B^4$, and $B^6$ (basal). The Fe–O bond lengths $B^2$ and $B^5$ increase for Fe-interstitial doping, whereas the basal ones decrease. Due to the induced O-vacancy, the dopant atom only forms bonds with five O-atoms in the $Fe^{2+}$ and $Fe^{3+}$ models. It's crucial to remember that the O-vacancy tends to pop up near the
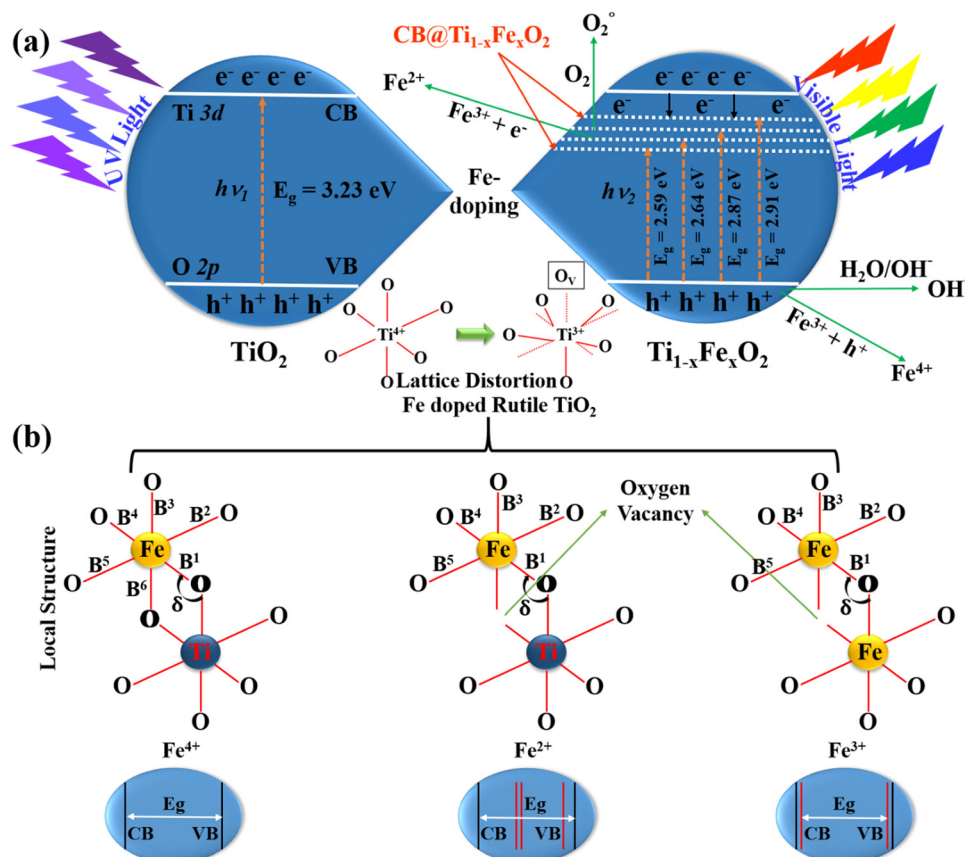
Fig. 1 (a) The process of charge transport involving elevated electrons and VBs of the $TiO_2$ nanorods with $Fe^{3+}$ ions of $Ti_{1-x}Fe_xO_2$ ($x = 0-0.1$), and (b) schematics of the local topologies of Fe-dopants in the different $Fe^{4+}$, $Fe^{2+}$, and $Fe^{3+}$ doped $TiO_2$ models respectively. $B^{1-6}$ are the bond lengths of Fe–O bonds and $\delta$ is the bond angle between Fe–O–Ti and Fe–O–Fe.

Fe-octahedron basal. Only $B^2$ and $B^5$ of these five Fe–O bond lengths remain comparable to one another, with the other three turning inequivalent. These findings demonstrate that the O-vacancy distorts the $TiO_6$ octahedra more significantly than the dopant atom alone.[30]

The first DSSC was fabricated by using a Pt counter electrode (CE), while the nanocrystals of $TiO_2$ were used as the photo-anode, which showed a PCE of 7.9%. Rawling *et al.* fabricated a DSSC using ruthenium-based dyes (N719) and reported a significant PCE of ∼12%.[31] Recently in 2019, Gratzel reported 12.3% PCE with a DSSC having cobalt(ɪɪ/ɪɪɪ)-based electrolyte, platinum (Pt) CE, and $TiO_2$ photo-anode. However, the corrosive degradation of Pt by electrolytes having $I^-/I_3^-$ ions and very high prices hinder its applicability.[32] Record 14.2% PCE is achieved with a novel thieno[3,2-*b*]indole-type organic dye having a suitable porphyrin sensitizer, where the used redox electrolyte is $[Co(bpy)_3]^{2+/3+}$.[33] To add a modified layer over the FTO, different types of advanced coating techniques such as chemical vapor deposition,[34] sputtering,[35] spray pyrolysis[36] and dip coating[37] are preferred.

In this work, we preferred the easy and suitable spin-coating deposition method to make DSSCs cheaper and more efficient. An ideal dye for DSSCs will have a large light absorption range, a large number of oxygen functional groups, a large molar

extinction coefficient, and high stability. Also, for effective photo-electron injection, the energy level of the dyes should meet the conduction band of the photoanode.[38–41] However, disadvantages associated with inorganic dyes, such as low yield, hazardous nature, and long extraction process, hinder their applicability.[42] To overcome this, natural dyes are generally preferred because of their cost-effectiveness, easy biodegradation, and wide availability. Natural dyes are generally extracted from the various parts of the plants, like fruits, flower petals, peels, leaves, *etc.*[43] Continuous progress in the field of natural and metal complex dye-based DSSCs revealed a significant performance ∼ 0.1–10.3%.[44–46] The most common pigments that are found in these dyes are (i) betalains, (ii) flavonoids, (iii) chlorophyll, and (iv) carotenoids. DSSCs support the development of photovoltaic components with high conversion efficiency and low costs in a system for converting pure and non-conventional solar radiation into electricity. When assessing the performance of DSSCs, the dyes role as a sensitizer is very crucial. Due to their low cost, high availability, and biodegradability, natural dyes (organic dyes) have become a worthwhile alternative to the typical and expensive inorganic sensitizers.

Herein, we used betalain pigments as a natural photosensitizer to perform the DSSC investigation. The group of red-violet (betacyanins) and yellow (betaxanthins) pigments known as

betalains is found in the Caryophyllales plants. Red beetroot is one of the propitious sources of the betalain pigments, which belongs to the subfamily Betoideae of the family Amaranthaceae. Red beetroot altogether contains two major soluble pigments, betanin (red) and vulgaxanthine I (yellow). Depending on the cultivar, red beetroots betacyanin and betaxanthin contents vary between 0.04 and 0.21% and 0.02 and 0.14%, respectively. However, certain new varieties generate higher betalain amounts. Recently many researchers have investigated betalain pigments for DSSC applications and reported that the device performance is directly associated with the dye's adaptability. Betalain pigments typically absorb visible light ranging from 476 to 600 nm, with maximum absorption at 537 nm at pH 5.0. Since the red beetroot's betalain spectrum is primarily restricted to betanin, colour variation is minimal. Moreover, the chemical stability of betalain pigments is also a concern for highly efficient DSSCs. pH variation, higher oxygen level storage, light intensity, water activity, and high-temperature exposure will significantly degrade the betalain pigments. To avoid any degradation, we have immediately used the extracted dyes and kept them at 4 °C throughout the dye loading process. In addition, considering the non-toxicity, low cost, and ease of synthesis of $TiO_2$ photoanodes, we aimed to develop a very economical, efficient, and stable DSSC utilizing BV dyes and $Ti_{1-x}Fe_xO_2$ photoanodes. After carefully investigating the properties of hydrothermally grown novel $Ti_{1-x}Fe_xO_2$ nanobrushes, this study aims to reveal the performance enhancement of the DSSC utilizing natural betalain pigments extracted from BV. Physicochemical characterization of the synthesized $Ti_{1-x}Fe_xO_2$ photo-anodes has been done by XRD, XPS, FESEM, HRTEM, EIS, UV-Visible Spectroscopy, FT-IR analysis, and Raman analysis, and later the device characterization is done by $J–V$ analysis. The results of this work assisted us in extending our investigation further for natural DSSCs and other photovoltaic technologies comprising such types of novel nanostructured photoanodes. We believe that this work potentially contributes to the available literature and has enormous capabilities to cater to small and generic energy needs such as in wearables and thermochromic applications.

# 2. Experimental details

### 2.1. Materials

The materials used are as follows: transparent and conducting fluorine doped tin oxide (FTO) (Sigma Aldrich), $Ti(acac)_2OiPr_2$ (75% in isopropanol, Sigma Aldrich), 1-butanol ($\geq$99.4%, Sigma Aldrich), $Ti(OBu)_4$ ($\geq$97%, Sigma Aldrich), iron nitrate nanohydrate ($\geq$98%, Sigma Aldrich), DI water, Beta vulgaris dye, HCl (35% w/w), ethylene glycol ($\geq$99%, Sigma Aldrich), ethanol (Sigma Aldrich), Ni-based CE, KI ($\geq$99%, Sigma Aldrich), and $I_2$ ($\geq$99.8%, Sigma Aldrich). All chemical compounds were utilized as purchased without any additional purification.

### 2.2. TiO₂ compact layer (c-TiO₂) synthesis

Initially, 0.1 and 0.2 M solutions of $TiO_2$ were prepared separately for compact layer synthesis by using respective amounts

of $Ti(acac)_2OiPr_2$ in a 1-butanol solvent. For dissolving the precursor and obtaining a homogeneous solution, the mixture was stirred for 30 minutes at 27 °C. After preparing the desired solution, 0.1 M solutions was spin-coated once on the FTO substrate of 1.5 × 1.5 $cm^2$ batch size, followed by heating at 120 °C. Prior to spin coating, all the FTO substrates were cleaned in an ultra-sonicator using DI water, acetone, and ethanol for 15 minutes each, and then finally dried in air at 27 °C. Once the 0.1 M coating and heating for 30 minutes were completed, 0.2 M solution was spin-coated twice following the same process of 0.1 M coating. All the samples were annealed in an oven at ∼500 °C for 30 minutes after coating and c-$TiO_2$ was formed, which was later used to grow Fe-doped $TiO_2$ NRs.

### 2.3. Photoanode preparation

Self-organized and vertically grown bare and Fe-doped $TiO_2$ NRs were prepared directly on the FTO *via* a simple hydrothermal method. HCl (37%) and de-ionized water were mixed together in a 1 : 1 volume ratio and stirred on a magnetic stirrer at 27 °C for nearly 5 minutes and then 0.8 ml of $Ti(OBu)_4$ precursor was added. This solution was further stirred for 1 hour after mixing the different amounts of $Fe^{3+}$ ions ($Ti_{1-x}Fe_xO_2$, x = 0–0.1) and then the homogeneous solution was transferred into a 90 ml Teflon liner and packed in a stainless-steel autoclave. Vertically aligned $Ti_{1-x}Fe_xO_2$ NRs were synthesized on the c-$TiO_2$ layer coated FTO by direct immersion into the prepared solution and heat treated for 8 hours at 150 °C. After taking out the samples from the autoclave, they were washed with DI water and dried in air. Further to enhance the crystallinity and eliminate the residual organics, the samples were annealed at 450 °C for 30 minutes.

### 2.4. Dye extraction

Peeled-out BVs were taken to extract the natural dye for DSSC testing. The core of the BV was washed separately with DI water and ethanol and sonicated for 5 minutes each. Then it was dried in air at room temperature and cut down into small pieces, which were crushed later and mixed with lab-grade extra pure ethanol. The mixture was centrifuged to separate out the solid parts that remain in the mixture and filtered. The extracted liquid dye is again heated to evaporate the solvent and to get the appropriate viscous liquid dye.

### 2.5. Preparation of the electrolyte

A 5 mM solution of potassium iodide and iodine crystal was prepared in 5 ml of ethylene glycol solvent. The solution was suitably stirred for 1 hour at room temperature in a dark room and kept covered with aluminum foil to prevent direct exposure to solar radiation.

### 2.6. DSSC fabrication

The fabricated bare and Fe-doped $TiO_2$ photo-anodes and nickel (Ni) CE were sandwiched together to form a DSSC module. All the photo-anodes were dipped overnight in the extracted liquid from red BV for dye sensitization and little change in colour from milky white to reddish has been seen.

Ni-foam is pressed with a hydraulic press, sonicated in DI water for 5 minutes, and then dried in air at room temperature. The DSSC is assembled with the dye-sensitized photo-anode and Ni-CE one above each other in such a way that only coated part of the substrates was covered with the CE so that there will be some space left for the outer circuit connection. In between the photo-anode and Ni-CE, two drops of the prepared electrolyte were dropped. This assembly of the photo-anode and CE was fixed by two binder clips to hold the device gently. Negative and positive terminals of the fabricated device are the dye-sensitized $Ti_{1-x}Fe_xO_2$ (photoanode) and Ni-CEs, respectively, which are used to connect the outer circuit.

### 2.7. Characterization

The structure and composition of the bare and Fe-doped $TiO_2$ $NR_S$ were studied with an X-ray diffractometer (XRD, Empyrean, Malvern Panalytical X-ray diffractometer) with Cu Kα radiation ($\lambda = 1.5404$ Å). XRD studies were performed between $2\theta = 20°$ and $70°$. Absorption and band edge evaluation of the bare, Fe-doped $TiO_2$, and extracted dye was performed using a UV-Visible spectrophotometer (Shimadzu, UV-2600). Field Emission Scanning Electron Microscopy (FESEM, JEOL, JSM-7610 F plus) was used to determine the surface morphology and size of grown nanorods. Transmission electron microscopy (TEM) images of synthesized Fe-doped $TiO_2$ $NR_S$ were obtained using a JEOL JEM-F200 TEM operating at an accelerating voltage of 80 kV. X-ray photoelectron spectroscopy (XPS) of $Ti_{1-x}Fe_xO_2$ ($x = 0–0.1$) NRs was performed using a Kratos AXIS spectrometer with an Al $K_\alpha$ source ($h\nu = 1486.6$ eV). FTIR spectra of the extracted red beetroot dye in the range of 4000–400 $cm^{-1}$ were observed using a BRUKER TENSOR 27 spectrometer. Raman analysis was performed by using a H J Y micro-Raman spectrometer equipped with a He–Ne laser of 633 nm, and Raman spectra were recorded. Lastly, the photocurrent–voltage ($I$–$V$) characteristic curves were simulated using a solar simulator (#SS50AAA: PET Photo Emission Tech., INC) under standard 1 sun (AM 1.5G) illumination.

## 3. Results and discussion

### 3.1. X-Ray diffraction (XRD)

Fig. 2 displays the XRD patterns of $Ti_{1-x}Fe_xO_2$ ($x = 0–0.1$) NRs grown on the FTO substrate. XRD results of bare $TiO_2$ NRs match with the JCPDS card no. 21-1276, designated as the tetragonal rutile phase. Diffraction peaks observed at 26.69°, 27.61°, 36.25°, 37.90°, 41.41°, 54.60°, and 61.66° are assigned to (110), (121), (101), (200), (111), (211), and (002) planes, respectively, in pure $TiO_2$ NRs, showing crystalline nature.[47] There is no extra diffraction peak for Fe, which suggests that Fe content is below the detection limit and has nearly equal ionic radii. The $Fe^{3+}$ ions are well substituted in the $TiO_2$ crystal lattice and interstitials or $Ti^{4+}$ lattice sites. This indicates that $Fe^{3+}$ ions were strongly integrated homogeneously in the NR matrix and no Fe-oxide is present on the top of the surface, also discussed in the literature.[48,49]
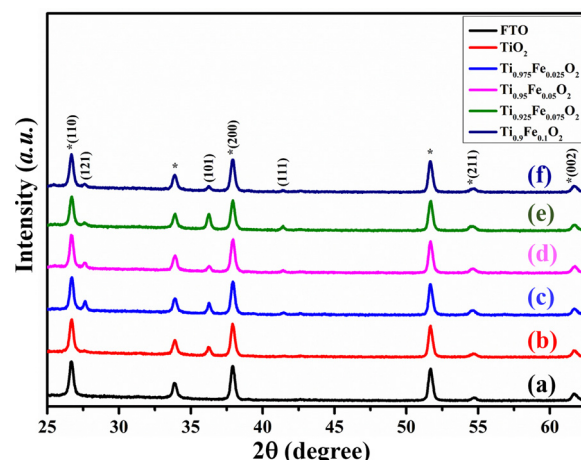


**Fig. 2** XRD patterns of the (a) FTO, (b) bare $TiO_2$, (c) $Ti_{0.975}Fe_{0.025}O_2$, (d) $Ti_{0.95}Fe_{0.05}O_2$, (e) $Ti_{0.925}Fe_{0.075}O_2$, and (f) $Ti_{0.9}Fe_{0.1}O_2$ $TiO_2$ NRs, respectively. * represents FTO peaks.

**Table 1** Variation in the lattice constant values with different concentrations of Fe-doping in $TiO_2$ NRs

| Composition | $a = b$ (Å) | $c$ (Å) |
| --- | --- | --- |
| $TiO_2$ | $4.864 \pm 0.003$ | $3.078 \pm 0.005$ |
| $Ti_{0.975}Fe_{0.025}O_2$ | $4.87 \pm 0.007$ | $3.08 \pm 0.004$ |
| $Ti_{0.95}Fe_{0.05}O_2$ | $4.874 \pm 0.004$ | $3.084 \pm 0.002$ |
| $Ti_{0.925}Fe_{0.075}O_2$ | $4.881 \pm 0.006$ | $3.085 \pm 0.001$ |
| $Ti_{0.9}Fe_{0.1}O_2$ | $4.890 \pm 0.002$ | $3.086 \pm 0.003$ |

The (100) and (200) plane domination over other planes indicates the preferential growth of NRs along the other direction perpendicular to the substrate. The lattice constant for undoped $TiO_2$ NRs is $a = b = 4.864 \pm 0.003$ Å and $c = 3.078 \pm 0.005$ Å, in good agreement with the available literature. Table 1 comprises the lattice constants for Fe-doped $TiO_2$ NRs and clear variations have been seen. A very small lower angle peak shift at 61.66° with increasing $Fe^{3+}$ ion concentration has been observed; that is, substitutional sites of $Ti^{4+}$ in the $TiO_2$ crystal were occupied by $Fe^{3+}$ ions. This is in good agreement with the lattice expansion as $2\theta$ angle increases, ascribed to the larger ionic radius of $Fe^{3+}$ (0.79 Å) than the $Ti^{4+}$ (0.75 Å).[50]

### 3.2. Surface morphology

Fig. 3 represents the FESEM images of $Ti_{1-x}Fe_xO_2$ ($x = 0–0.1$) NRs prepared at 150 °C for 8 h. On the top of the FTO substrate, a uniform compact-$TiO_2$ layer was coated and then $Ti_{1-x}Fe_xO_2$ NRs were grown vertically on the FTO substrate. Fig. 3(a) shows the top view of bare $TiO_2$ NRs, where the sides of the NRs are very smooth but there were few step edges mounted on the top. The growth of $TiO_2$ NRs may be due to additional Ti nucleation sites at the top step edges.[51] As expected, the obtained NRs have a tetragonal crystal structure with square facets as shown in Fig. 3(a). Also Fig. 3(a)–(e) validates the porous structure formation with interlinked $TiO_2$ NRs. Different concentrations of Fe-doping will change the morphology drastically as shown in Fig. 3(b)–(e).
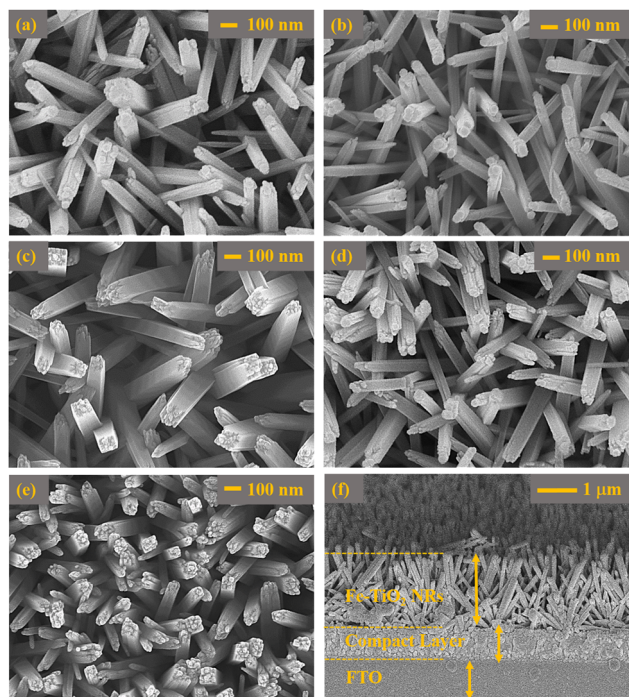
**Fig. 3** (a)–(e) FESEM top view image of $Ti_{1-x}Fe_xO_2$ (x = 0–0.1) NRs grown. (a) Undoped (x = 0) $TiO_2$ NRs, (b) x = 0.025, (c) x = 0.05, (d) x = 0.075, and (e) x = 0.1 and (f) cross-sectional image of undoped $TiO_2$ NR arrays.

As obtained, there is a hierarchical nano-dot-like structure grown on the top of the $TiO_2$ NRs. These nano-dot-like structures on the top of NRs will increase the surface area significantly and boost the change transfer ability. The average calculated length and diameter of the $Ti_{1-x}Fe_xO_2$ NRs from Fig. 3(a)–(e) are in the range of 350 ± 10 to 370 ± 10 nm and 80 ± 10 to 90 ± 10 nm, respectively, for x = 0–0.1. In Fig. 3(f), a cross-sectional view of the photoanode is shown and the average widths of $Ti_{1-x}Fe_xO_2$ NRs and c-$TiO_2$ layer are found to be nearly 1.4–1.9 μm and 250 nm, respectively. Reports are well suited and already explained the advantages of the semiconducting nanoscale NRs, such as (i) high surface-to-volume ratio,[52] (ii) very low grain boundaries, which directly alter the charge carrier trapping and scattering,[53] and (iii) suitable charge carrier transportation.[54] To escalate the dye loading, amply packed, large, and lean NRs-like dye scaffolds by maintaining enough charge carrier collection are required.[53] With Fe doping the rod-like morphology altered to a highly porous surface consisting of nanorod cum dot-like morphology, which indicated the increase in surface area, which may significantly change the charge conversion/extraction efficiency.

Transmission electron microscopy (TEM) investigation was performed to analyze the crystal structure of $TiO_2$ NRs. Low-resolution TEM images of single TiO2 NRs are represented in Fig. 4(a). It is surprising that there are numerous step edges present on the top facet of each NR as shown in Fig. 4(a). These step edges act as nucleation sites and results in the axial growth of $TiO_2$ NRs with different growth rates. Further, such step edges may act as substrates for the secondary growth of $TiO_2$



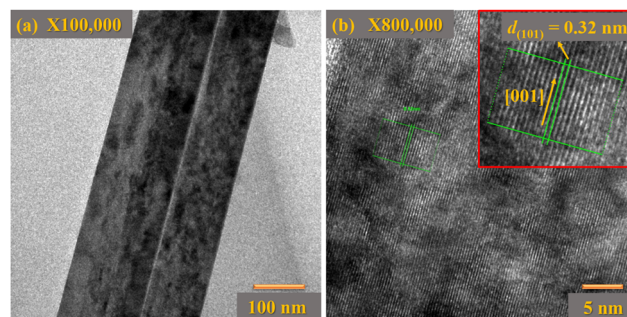**Fig. 4** (a) TEM images of a single $TiO_2$ NR, and (b) the corresponding HRTEM image of a single $TiO_2$ NR. The inset image of (b) displays the lattice spacing between (101) planes of rutile phase $TiO_2$.

NRs. The relative HRTEM image of a single $TiO_2$ NR is depicted in Fig. 4(b), which confirms the single crystalline behaviour of these $TiO_2$ NRs having a lattice spacing of 0.32 nm along (101) planes of tetragonal rutile $TiO_2$ NRs. Additionally, the growth direction of $TiO_2$ NRs was parallel to the normal of the (001) plane. Therefore, the rutile $TiO_2$ NR arrays grow predominantly along the [001] plane, showing good agreement with the XRD pattern.

### 3.3. X-ray photoelectron spectroscopy (XPS)

$TiO_2$ has garnered a lot of interest across the globe since it is a well proven and excellent photoanode for DSSCs. On the other hand, $TiO_2$ is a wide-bandgap (3.2 eV) semiconductor and can absorb UV light very easily. Numerous researchers claim that metal cations and non-metal anions can successfully dope titanium dioxide to prevent this UV sensitization. In this work, simple and inexpensive hydrothermal fabrication of Fe-doped $TiO_2$ produced excellent photo-anodic characteristics for DSSC implementations. X-ray Photoelectron Spectroscopy (XPS) was employed to fully understand the doping processes. Basically, XPS is a technique that was used to investigate the elemental composition, chemical state, and ionic states of iron in $Ti_{1-x}Fe_xO_2$ (x = 0–0.1) photoanodes.

Survey spectra of bare $TiO_2$ and $Ti_{0.95}Fe_{0.05}O_2$ photoanodes are displayed in Fig. 5(a). From the survey scan, the presence of Ti, O, C, and Fe elements were identified, whereas no Fe content was detected in bare $TiO_2$ photoanodes. Here C is present in the survey scan, which is only because of the background, not present in the synthesized samples. Further high-resolution XPS spectra of Ti(2p) and O(1s) core levels from bare $TiO_2$ and $Ti_{0.95}Fe_{0.05}O_2$ photoanodes are shown in Fig. 5(b), (c) and (e), (f), respectively.

Fig. 5(b) and (e) reveals that the XPS spectrum of the Ti(2p) core consists of two major peaks, namely, $Ti(2p)_{3/2}$ and $Ti(2p)_{1/2}$, whereas the Ti(2p) spectrum mostly presents in $Ti^{4+}$ oxidation with the minor composition of $Ti^{3+}$ (because of O-inadequacy in the $TiO_2$ lattice) for both bare $TiO_2$ and $Ti_{0.95}Fe_{0.05}O_2$ photoanodes, respectively. In bare $TiO_2$ photoanodes, the binding energies of dominant $Ti(2p)_{3/2}$ and minor $Ti(2p)_{1/2}$ were observed at 457.8 and 463.3 eV (Fig. 5(b)). However, both these Ti(2p) spectrum peaks were shifted positively

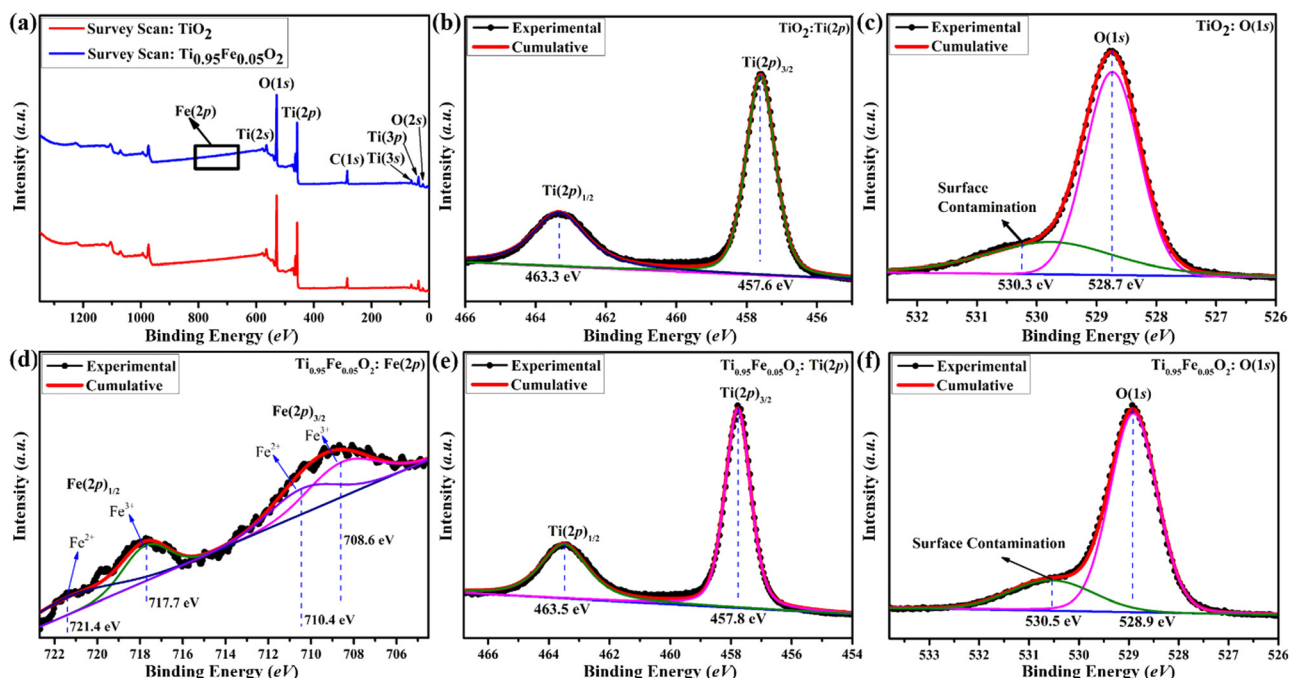**Fig. 5** The XPS spectra of bare $TiO_2$ and $Ti_{0.95}Fe_{0.05}O_2$ photoanodes. (a) Comparison of XPS survey scan spectra, (b) $TiO_2$: $Ti(2p)$ core-level XPS spectra, (c) $TiO_2$: $O(1s)$ core-level XPS spectra, (d) $Ti_{0.95}Fe_{0.05}O_2$: $Fe(2p)$ XPS spectra, (e) $Ti_{0.95}Fe_{0.05}O_2$: $Ti(2p)$ core-level XPS spectra, and (f) $Ti_{0.95}Fe_{0.05}O_2$: $O(1s)$ core-level XPS spectra.

by 0.2 eV in $Ti_{0.95}Fe_{0.05}O_2$ photoanodes (Fig. 5(e)). This peak shift is ascribed to reduced Ti-coordination, lowering of the Ti–O bonds; that is, the $Ti^{4+}$ content is decreased. Additionally, this peak shift led to the formation of Fe–O–Ti bonds attributed to $TiO_2/Fe_2O_3$ binary oxide formation.

High-resolution XPS spectra of $O(1s)$ for bare $TiO_2$ and $Ti_{0.95}Fe_{0.05}O_2$ photoanodes are shown in Fig. 5(c) and (f), respectively. Here in the case of bare $TiO_2$, the binding energy of the ruling $O(1s)$ peak is 528.7 eV, which later shows a minor positive shift of 0.2 eV in $Ti_{0.95}Fe_{0.05}O_2$ derivatives, ascribed to the oxygen signals in the $TiO_2$ lattice. Moreover, $O(1s)$ peaks are decreased in $Ti_{0.95}Fe_{0.05}O_2$ photoanodes as the Fe–O bond formation takes place on the $TiO_2$ surface. At both 530.3 and 530.5 eV binding energies in both cases another peak is observed, which is due to surface contamination, i.e., $OH^-$ adsorption on the $TiO_2$ surface.

Lastly, XPS spectra of $Fe(2p)$ were investigated to understanding the electronic behaviour of Fe in $Ti_{0.95}Fe_{0.05}O_2$ photoanodes and the core spectrum of $Fe(2p)$ can be seen in Fig. 5(d). The binding energy of two dominant $Fe(2p)_{3/2}$ and $Fe(2p)_{1/2}$ doubled peaks were found at 708.6 and 717.7 eV, respectively, which is associated with $Fe^{3+}$ oxides. Along with these main peaks, there are some shake-up satellite peaks, and weak peaks are also observed at 710.4 and 721.4 eV, respectively, which are identified as a minor portion of $Fe^{2+}$ oxidation states. However, these $Fe^{2+}$ ions present on the $TiO_2$ surface may lose their changeability to $Fe^{3+}$ ionic state and lead to the formation of $Ti^{3+}$ defect states. The collected information will be very helpful for transition metal-based $TiO_2$ doping processes in the future.

### 3.4. UV-Visible characterization

Below 400 nm, absorption spectra (Fig. 6(a)) of $Ti_{1-x}Fe_xO_2$ ($x = 0$–0.1) NRs show a sudden increase in absorption, assigned to stable rutile $TiO_2$ with the bandgap of 3.2 eV ($x = 0$, $TiO_2$ NRs).[55] In the visible region, a nearly non-zero baseline is depicted, which matches with the previously reported work of Zhao *et al.*[56] This may happen due to the low film thickness or pinholes present in the film. The absorbance of iron ions is present in the spectra of Fe-doped $TiO_2$ NRs.

In Fig. 6(b), optical bandgap estimation is shown from the Tauc plot, and observed bandgaps for $Ti_{1-x}Fe_xO_2$ ($x = 0$–0.1) NRs are 3.23, 2.91, 2.87, 2.64, and 2.59 eV, respectively. From the Tauc plot, there is a red shift in all Fe-doped samples. This red shift can be attributed to Fe 3d electron excitation to the $TiO_2$ conduction band. Shallow trap formation between the conduction and valence bands of $TiO_2$ NRs by Fe doping was confirmed in the literature, which may be responsible for the increasing bandgap with increasing Fe concentration.[57] The UV-Visible analysis of the prepared dye from BV is represented in Fig. 6(c). In fact, dyes have control over the photo charge generation and transportation simultaneously and on the resulting device performance as well. To investigate the light capture ability of the used dye, UV-Vis spectroscopy was performed. A broad absorption band at 427–523 nm is observed and the maximum absorption is found at $\sim$457 nm. The maximum absorption peak ($\sim$457 nm) is attributed to the purple-red betanin presence, while a small hump observed at $\sim$451 nm confirms the presence of yellow betaxanthin pigments, showing good agreement with the available literature.
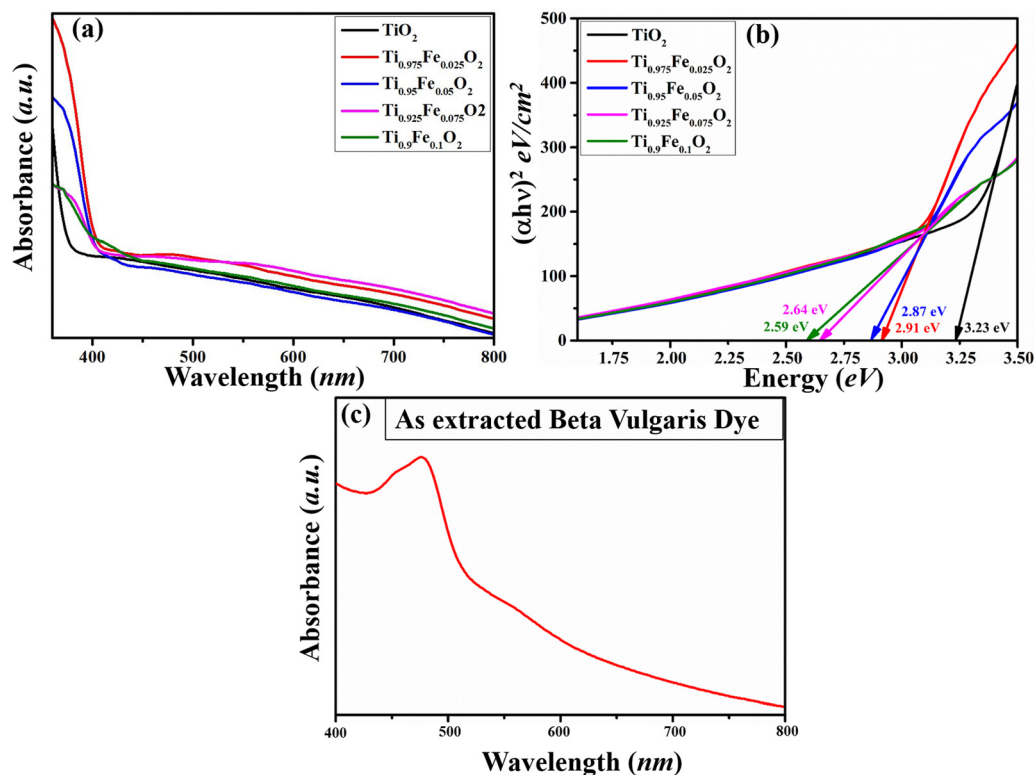
**Fig. 6** Absorption spectra of (a) $Ti_{1-x}Fe_xO_2$ ($x = 0-0.1$) NRs, (b) Tauc plot of the $Ti_{1-x}Fe_xO_2$ ($x = 0-0.1$) NRs and (c) UV-Visible spectra of the extracted BV dye.

Functional groups that are present in the dye, mainly –O═H and –C(═O)OH, will boost the charge transfer at the dye and photoanode interface. Approximately 3.79 eV photon energy is required to excite the electron from the HOMO to the LUMO states of the BV dye.

### 3.5. FT-IR spectroscopy

The presence of functional groups in the dye extracted from natural resources is necessary for the dye adsorption over the $TiO_2$ NR photoanode. The FTIR spectrum of the dye extracted from BV is shown in Fig. 7, which confirms the presence of
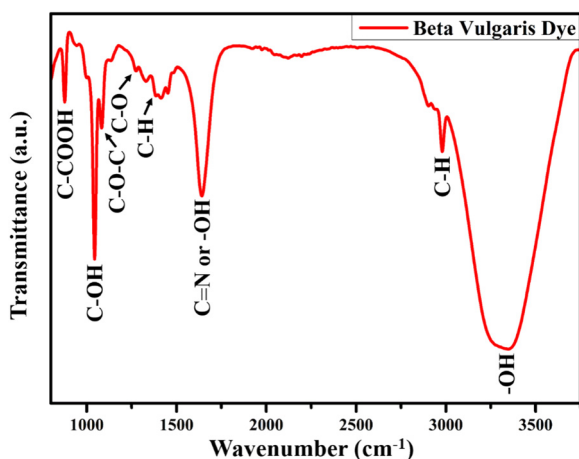
betalain pigments. Optimized FT-IR results have shown a sharp peak at $3346 \text{ cm}^{-1}$ because of stretching vibration, whereas the peak at $2978 \text{ cm}^{-1}$ is assigned to the C–H stretching vibration of alkanes. At $1637 \text{ cm}^{-1}$, the amide bond carbonyl stretching mode absorption band is found. The peak at $1376 \text{ cm}^{-1}$ is attributed to either the C–N stretching or –OH vibrational bonds, while the C–O bond is assigned at $1272 \text{ cm}^{-1}$ for carboxylic acid stretching vibration mode. Other than these modes, symmetric stretching vibration (C–O–C), C–H bond deformation, and C–COOH bond stretching vibration absorption bands are found at 1086, 1042, and $876 \text{ cm}^{-1}$, respectively. All these observed vibrational and stretching modes corresponding to the different functional groups are associated with the red-purple betanin pigments and effectively bound with the photoanode surface.[58]

### 3.6. Raman spectroscopy

Generally, Raman spectroscopy (Fig. 8) is preferred to investigate the structural properties of the hydrothermally grown $Ti_{1-x}Fe_xO_2$ ($x = 0-0.1$) NRs. All the first-order three active Raman modes $A_{1g}$ ($609.18 \text{ cm}^{-1}$), $B_{1g}$ ($143.65 \text{ cm}^{-1}$), and most prominent second-order scattering mode $E_g$ ($446.37 \text{ cm}^{-1}$) validate the formation of rutile phase $TiO_2$ NRs. At near $140 \text{ cm}^{-1}$, a sharp peak occurs because of O–Ti–O symmetric bending vibration causing $B_{1g}$ mode. Another intense characteristic peak at $446 \text{ cm}^{-1}$ was observed, which may be attributed to symmetric O–Ti–O stretching vibration. All the results are in good agreement with previously reported literature.
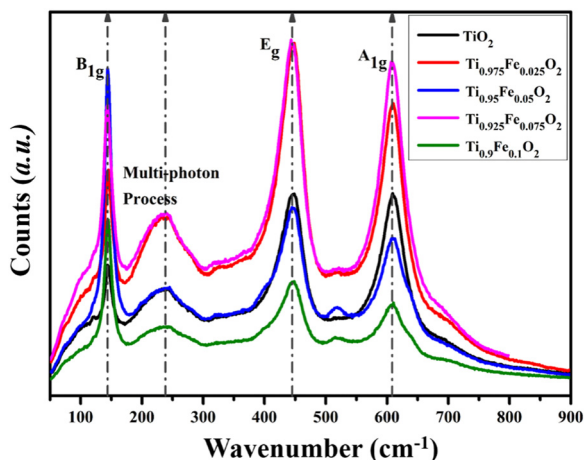


**Fig. 7** FT-IR spectrum of the dye extracted from the BV.

**Fig. 8** Raman spectra for tetragonal rutile phase $Ti_{1-x}Fe_xO_2$ ($x$ = 0–0.1) NRs grown hydrothermally on the FTO substrate.

## 4. Working mechanism

The working mechanism of a DSSC is mainly attributed to four pillars: photo-absorption, electron injection, charge carrier transportation, and current collection. The schematic shown in Fig. 9 addressed these attributes and represents the photoconversion of light into current. First, photons are absorbed by betalain pigments used as the photosensitizer and this will lead to electron excitation from the valence state ($S^+/S$) to the conduction state ($S^+/S^\star$) of the dye. Fig. 6(c) shows the highest absorption peak of the dye near 457 nm, while the minimum photo energy required for electron excitation is nearly 3.79 eV. The excited electrons having lifetimes in the range of nanoseconds were injected into the $TiO_2$ NR conduction band, which is generally lower than the excited state of the dye. There is also a little absorption of photons by $TiO_2$ NRs in the UV region as reported in the literature.[59] This will result in oxidation of the dye and can be represented by the equation is given below,
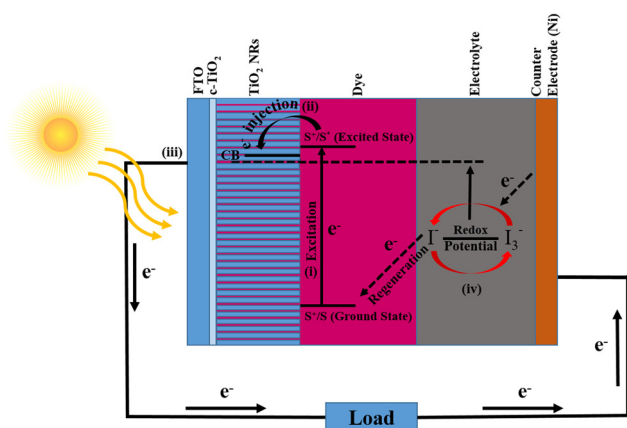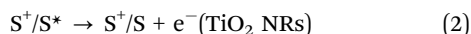
$$S^+/S + h\nu \rightarrow S^+/S^\star \tag{1}$$

$$S^+/S^\star \rightarrow S^+/S + e^- (TiO_2 \text{ NRs}) \tag{2}$$



**Fig. 9** Typical schematics and working of the dye sensitized solar cells.

Now, these injected charge carriers (electrons) were transported *via* $TiO_2$ NRs and diffused to the transparent conducting electrode (FTO). Later, the electrons reached the CE *via* external circuitry. At the CE, the electrons were reduced from $I_3^-$ to $I^-$ and due to the electron acceptance from the $I^-$ ion redox mediator, dye regeneration takes place. Subsequently, the oxidation of $I^-$ into $I_3^-$ (oxidized state) takes place (eqn (3)).

$$S^+/S^\star + e^- \rightarrow S^+/S \tag{3}$$

$$I_3^- + 2e^- \rightarrow 3I^- \tag{4}$$

Further, diffusion of the $I_3^-$ oxidation mediator at the CE takes place and reduces into I ions (eqn (4)). Hence, as explained, dye sensitization happens when the sunlight is illuminated and the formation of the HOMO and LUMO will take place. If the sunlight radiation has sufficiently large energy, then the $e^-$ charges are excited and injected into the CB of $Ti_{1-x}Fe_xO_2$ ($x$ = 0–0.1) NRs, and simultaneously the dye will oxidize. Outer circuitry helps these injected charges reach the CE. The electrolyte having $I^-$ and $I_3^-$ redox ions gets reduced by the injected electrons, which will lead to the regeneration of the dye molecules.

## 5. Photovoltaic performance

The photovoltaic properties of the DSSC device prepared using $Ti_{1-x}Fe_xO_2$ ($x$ = 0–0.1) NRs grown on the FTO substrate having a $TiO_2$ blocking layer sandwiched in between are shown in Fig. 10(a). Betalain pigments extracted from BV (red beetroot) were used as photosensitizers. For its real-world applications, the device's stability is a priority in addition to performance. After 300 hours of testing, 70% PCE retention was found in the DSSCs composed of the most effective $Ti_{0.95}Fe_{0.05}O_2$ photoanodes and BV dyes. Further, the PCE retention of the DSSCs having $TiO_2$, $Ti_{0.975}Fe_{0.025}O_2$, $Ti_{0.925}Fe_{0.075}O_2$, and $Ti_{0.9}Fe_{0.1}O_2$ photoanodes was 50, 67, 60, and 45%, respectively, after 300 hours under the standard 1 sun (AM 1.5G) illumination as shown in Fig. 10(b).

The incident photon conversion efficiency (IPCE) investigation of the corresponding DSSCs is depicted in Fig. 10(c) in the wavelength range from 350 to 750 nm. The greatest IPCE value, 54.6% of the $Ti_{0.95}Fe_{0.05}O_2$ photoanodes, was reported at ~560 nm. However, for the $Ti_{0.925}Fe_{0.075}O_2$, $Ti_{0.9}Fe_{0.1}O_2$, $Ti_{0.975}Fe_{0.025}O_2$, and pure $TiO_2$ photoanodes, the maximum obtained IPCE peak values are 48.3, 43.5, 39.9, and 34.6%. The IPCE value and $J_{SC}$ had a favourable correlation. Consequently, the results of the $J$–$V$ study and the overall IPCE investigation were consistent. The absorbance of the betalain dye occurred between 400 and 600 nm, where the IPCE value was maximum. On the other hand, absorption of $Ti_{1-x}Fe_xO_2$ ($x$ = 0–0.1) photoanodes varied between 350 and 450 nm related to the bandgap of 2.59–3.23 eV, which were properly compatible with the IPCE study findings.

The large IPCE values for the $Ti_{0.95}Fe_{0.05}O_2$ photoanode-based DSSCs over a huge spectrum will increase the light-harvesting capacity, which is ascribed to the massive dye
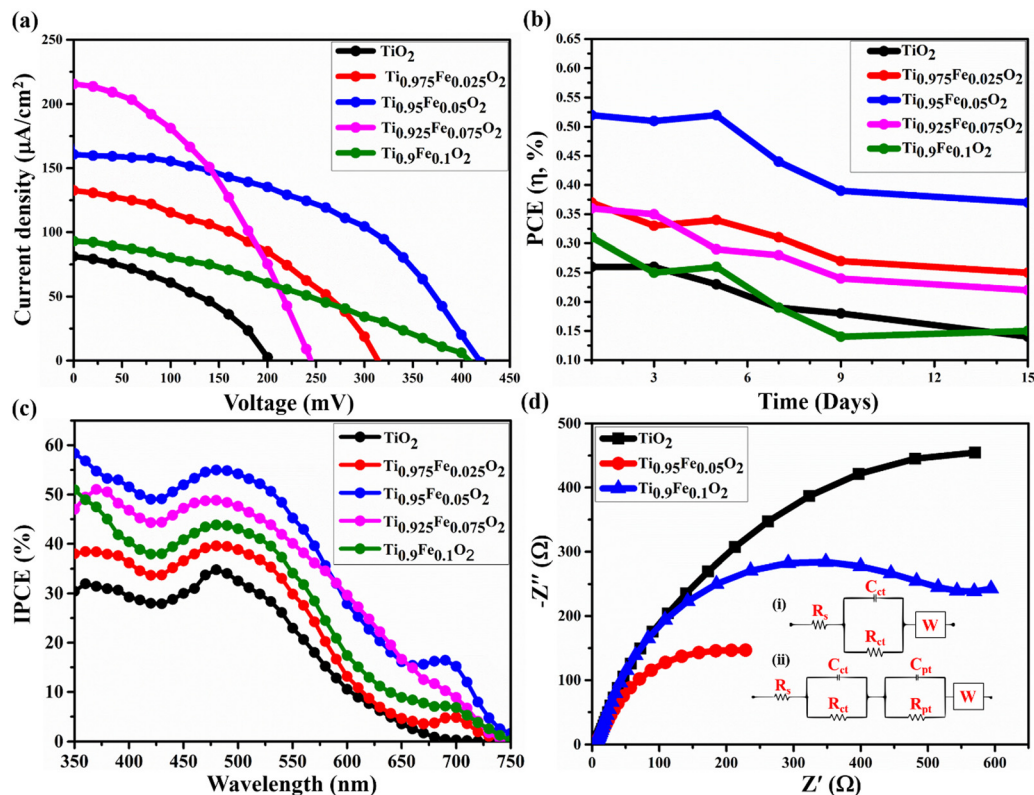
**Fig. 10** (a) $J$–$V$ characteristics of the $Ti_{1-x}Fe_xO_2$ ($x = 0$–0.1) NR-based DSSC utilizing BV dyes as sensitizers, and (b) stability analysis of the fabricated DSSCs consisting of $Ti_{1-x}Fe_xO_2$ ($x = 0$–0.1) photoanodes and BV dyes. (c) IPCE spectra of $Ti_{1-x}Fe_xO_2$ ($x = 0$–0.1) NR photoanode-based DSSCs. (d) EIS Nyquist plots of undoped and doped $TiO_2$ photoanodes at a bias of $V = V_{OC}$.

loading and maximum reflectance. Additionally, it is discovered from IPCE analysis that the $Ti_{0.95}Fe_{0.05}O_2$ photoanode-based DSSCs exhibit a clear red-shift to a higher wavelength in comparison to others due to the efficient light scattering properties.

The Electron Impedance Spectroscopy (EIS) investigation of the $Ti_{1-x}Fe_xO_2$ ($x = 0$–0.1) photoanode-based DSSC in the frequency range 0.1 Hz to 100 kHz is shown in Fig. 10(d). EIS evaluates the charge transfer mechanisms in DSSCs, such as series resistance $R_s$, related to the resistance offered by FTO and CE, high-frequency impedance responses $R_{ct}$ and $C_{pt}$ associated with the events happening at the Ni/electrolyte interface, mean frequency responses $R_{pt}$ and $C_{pt}$ related to the electron transport and recombination at the $TiO_2$/electrolyte interface, and low-frequency response $W$ designated as electrolyte diffusion impedance.

As depicted in Fig. 10(d), in the mean frequency region, the Nyquist plots contain a semicircle, which is ascribed to the $TiO_2$/electrolyte interfacial electron transport resistance and recombination. However, a very small straight line at low frequency is associated with diffusion mechanics. The diameter of different semicircles featured in the Nyquist plot of $Ti_{1-x}Fe_xO_2$ ($x = 0$–0.1) photoanodes changed with the varying concentration of Fe. Equivalent circuits for bare $TiO_2$ and $Ti_{0.9}Fe_{0.1}O_2$ photoanodes are represented in the inset circuit (i) drawn. However, the equivalent circuit for the $Ti_{0.95}Fe_{0.05}O_2$

photoanode is represented in the inset circuit (ii). All the values of $R_s$, $R_{ct}$, $C_{ct}$, $R_{pt}$, $C_{pt}$, and $W$ for $Ti_{1-x}Fe_xO_2$ ($x = 0$–0.1) photoanode-based DSSCs are summarized in Table 3. Finally, the $Ti_{0.95}Fe_{0.05}O_2$ photoanode has two impedance components with smaller amounts of electron transport resistance, such as $R_{ct} = 660\ \Omega$, which indicates a decrease in electron recombination and an effective enhanced electron transport, leading to higher conductivity, compatible with the previous findings.

**Table 2** Photovoltaic studies of the $Ti_{1-x}Fe_xO_2$ ($x = 0$–0.1) photoanode-based DSSC utilizing BV dyes as light harvesters

| Composition | $J_{SC}$ (mA cm$^{-2}$) | $V_{OC}$ (mV) | FF | $\eta$ (%) |
|---|---|---|---|---|
| $TiO_2$ | 0.080 | 203 | 0.97 | 0.26 |
| $Ti_{0.975}Fe_{0.025}O_2$ | 0.151 | 420 | 0.36 | 0.37 |
| $Ti_{0.95}Fe_{0.05}O_2$ | 0.130 | 312.3 | 0.79 | 0.52 |
| $Ti_{0.925}Fe_{0.075}O_2$ | 0.210 | 246 | 0.43 | 0.36 |
| $Ti_{0.9}Fe_{0.1}O_2$ | 0.092 | 419 | 0.50 | 0.31 |

**Table 3** Corresponding circuit parameters of $Ti_{1-x}Fe_xO_2$ ($x = 0$–0.1) photoanodes in 1 M KOH electrolyte

| Composition | $R_s$ ($\Omega$) | $R_{ct}$ ($\Omega$) | $C_{ct}$ (mF) | $R_{pt}$ ($\Omega$) | $C_{pt}$ (mF) | $W$ (mMho) |
|---|---|---|---|---|---|---|
| $TiO_2$ | 21.27 | 1376 | 37.69 | — | — | — |
| $Ti_{0.95}Fe_{0.05}O_2$ | 3.653 | 659.3 | 21.86 | 96.05 | 27.74 | 27.82 |
| $Ti_{0.9}Fe_{0.1}O_2$ | 9.236 | 991 | 42.98 | — | — | 22.43 |

**Table 4** Comparative study of the BV dye based DSSC performance from the available literature

| Dye | CE | Photoanode | $J_{SC}$ (mA cm$^{-2}$) | $V_{OC}$ (mV) | FF (%) | $\eta$ (%) | Ref. |
|---|---|---|---|---|---|---|---|
| BV | Carbon | ZnO | 0.72 | 460 | 0.54 | 0.1788 | 64 |
| Purple cabbage and BV | Carbon | ZnO | 1.12 | 560 | 0.60 | 0.3824 | |
| BV | Carbon | TiCl$_4$ treated TiO$_2$ | 2.23 | 407.6 | 0.54 | 0.49 | 65 |
| 80% BV + 20% spinach | Carbon | TiCl$_4$ treated TiO$_2$ | 4.65 | 386.7 | 0.55 | 0.99 | |
| BV | — | TiO$_2$ | — | — | 0.469 | 0.467 | 66 |
| Orange Bougainvillea + BV (1:1) | — | TiO$_2$ | — | — | 0.56 | 0.274 | |
| BV | Au | TiO$_2$ | | 223 | 0.66 | 0.096 | 67 |
| BV | | TiO$_2$ | 2.71 | 576 | 0.57 | 0.89 | 68 |
| BV + Tetraethylorthosilicate | Carbon | TiO$_2$ | 2.08 | 609 | 0.54 | 0.68 | |
| BV | Pt | TiO$_2$ | 1.295 | 380 | 0.32 | 0.15 | 69 |
| BV | Graphite | TiO$_2$ | 1.7 | 0.46 | — | 1.3 | 70 |
| BV | Pt | TiO$_2$ | 0.055 | 470 | — | 0.03 | 71 |
| BV | Nickel | TiO$_2$ NRs | 0.080 | 203 | 0.97 | 0.26 | This work |
| BV | Nickel | Ti$_{0.975}$Fe$_{0.025}$O$_2$ NRs | 0.151 | 420 | 0.36 | 0.37 | This work |
| BV | Nickel | Ti$_{0.95}$Fe$_{0.05}$O$_2$ NRs | 0.130 | 312.3 | 0.79 | 0.52 | This work |
| BV | Nickel | Ti$_{0.925}$Fe$_{0.075}$O$_2$ NRs | 0.210 | 246 | 0.43 | 0.36 | This work |
| BV | Nickel | Ti$_{0.9}$Fe$_{0.1}$O$_2$ NRs | 0.092 | 419 | 0.50 | 0.31 | This work |

In this study, we investigated the role of Ti$_{1-x}$Fe$_x$O$_2$ ($x$ = 0–0.1) photoanodes on the DSSC performance. Various solar cell performance parameters such as power conversion efficiency ($\eta$%), open circuit voltage ($V_{OC}$), short circuit current density ($J_{SC}$), and fill factor (FF) for the Ti$_{1-x}$Fe$_x$O$_2$ ($x$ = 0–0.1) based DSSC are given in Table 2. Performance improvement directly depends on (i) a large contact area between FTO and c-TiO$_2$ and (ii) the blocking ability of the c-TiO$_2$. A large contact area will significantly shrink the charge transport resistance and simultaneously increase the charge collection efficiency, while the blocking ability of c-TiO$_2$ will help to reduce the charge recombination.[60] The choice of CEs also plays an important role in the device performance.[61]

Here in this study, we preferred a Ni-based CE for its cost effectiveness, easy processing and significant performance. However, Ni has a lower conductivity of $1.43 \times 10^7$ S m$^{-1}$ as compared to conventional CEs such as gold ($4.10 \times 10^7$ S m$^{-1}$), silver ($6.30 \times 10^7$ S m$^{-1}$), copper ($5.96 \times 10^7$ S m$^{-1}$), *etc.*, resulting in the lower performance (as compared to some reports given in Table 4) of the Fe-doped TiO$_2$ NR photoanode and Ni-CE based DSSC, where the BV dye has been used as the photosensitizer. Apart from the lower conductivity of Ni-CE, the photo generated charge recombination at the FTO and c-TiO$_2$ interface will lead to a significant but lower efficiency of 0.52% only. However, the cost effectiveness and comparable PCE of the Ni-CE based DSSC make it an eco-friendly and affordable solar cell.

Table 2 confirms the considerable change from sample to sample, particularly in $J_{SC}$. $J$–$V$ results show that there is a significant increase in $J_{SC}$ accompanied by enhanced $V_{OC}$. Undoped samples have shown lower $J_{SC}$ because of fast photo-charge recombination, which is well explained in the available literature.[62] As the Fe concentration increases, the $J_{SC}$ values also increase simultaneously. This may have happened due to absorption enhancement and energy transport from the Fe$^{3+}$ energy band to the conduction band of the TiO$_2$ NRs. The PCE and $J_{SC}$ were nevertheless inhibited when too much Fe content was introduced because potential barriers stopped the electrons from flowing to the external circuit. Also, because of reduced grain boundary resistance, the recombination losses

are greatly reduced during charge transportation.[63] Hence, based on the realized photovoltaic properties, increased $\eta$ with the Fe-doping can be acknowledged.

A comparative study of BV dye-based DSSCs is discussed in Table 4. Herein, we also reported the performance of the Ti$_{1-x}$Fe$_x$O$_2$ NR-based DSSC by using betalain pigments extracted from BV. BV dyes were examined by Sinha *et al.* for DSSCs with the combination of carbon and ZnO electrodes and the obtained PCE was 0.17%. In the same report, a mixed dye (chlorophyll and betalains) successfully boosted the device performance by 0.38%.[64] In another report, Bashar *et al.* used TiCl$_4$-treated TiO$_2$ photoanodes for the DSSC having a BV photosensitizer and achieved 0.49% PCE, whereas by mixing red and green dyes (4:1), the performance was notably improved up to 0.99%.[65] Salinas *et al.* investigated combined BV and orange Bougainvillea extracts with a TiO$_2$ photoanode for DSSCs and obtained 0.274% PCE, while a bare BV dye showed a better PCE of 0.467%. This lowering of PCE with the mixed dye was ascribed to the lowering of photo-absorption.[66] Increased lifetime and a little lower PCE (0.89–0.68%) have been reported with mixed BV dye and tetraethylorthosilicate.[68]

Accumulatively, it was seen that the limited charge transfer capability and surface area coverage of TiO$_2$ photoanodes in combination with conventional CEs need to be modified for better performance. To acknowledge these gaps, we doped TiO$_2$ NRs with Fe, which tuned the absorption edges in the visible region and reduced the charge recombination at the FTO/c-TiO$_2$ interface. Having nearly equal ionic radii, Fe doping will maintain the crystal's structure. Enhanced surface adsorption and low energy level photonic excitation will be achieved with Fe doping.[18–24] Moreover, we replaced the costly conventional CE with Ni, which exhibited notable performance despite having lower conductivity.

## 6. Conclusions

In conclusion, we have prepared a very economical DSSC using Ti$_{1-x}$Fe$_x$O$_2$ nanorods and BV dyes. To understand the role of

Fe-doped $TiO_2$ photoanodes and BV dyes in DSSC performance, various physicochemical characterization studies and photo-voltaic analysis were performed. This Fe-doping will reduce the photo-charge recombination, while c-$TiO_2$ helps in minimizing the interfacial charge transfer resistance, which is a very effective approach to resolve the low PCE of the DSSCs. On the other hand, the cheaply prepared Ni-CEs will enhance the charge collection. Herein, this combination of photoanodes, dyes, and CEs were explored for the very first time and a notable PCE was reported. However, pinholes present on the photo-anode surface, and dye degradation may lead to device failure in later stages. Furthermore, ease of fabrication, cost-effectiveness, eco-friendly nature, and remarkable performance of the DSSC having Fe-doped $TiO_2$ NRs photoanodes, Ni-CEs, and betalain pigment-based photosensitizers make it an effective and possible approach for commercial fabrication. In addition, such DSSCs may become the game changer for some novel applications such as in wearables, thermochromics, and laser drilling.

## Data availability statement

The data that support the findings of this study are available from the corresponding author upon reasonable request.

## Author contributions

Abhishek Srivastava: conceptualization, validation, methodology, investigation, formal analysis, and writing-original draft. Jena Akash Kumar Satrughna: formal analysis. Manish Kumar Tiwari: formal analysis and editing. Archana Kanwade: writing-original draft. Subhash Chand Yadav: editing. Kiran Bala: formal analysis, writing-original draft and editing, and supervision. Parasharam M. Shirage: conceptualization, funding acquisition, resources, supervision, and writing- review& editing.

## Conflicts of interest

The authors declare no competing financial interests.

## Acknowledgements

## References

1 B. O'Regan and M. Gratzel, *Nature*, 1991, **353**, 737–740.

2 K. Kakiage, Y. Aoyama, T. Yano, K. Oya, J. Fujisawab and M. Hanaya, *Chem. Commun.*, 2015, **51**, 15894–15897.

3 L. Song, P. Du, J. Xiong, F. Ko and C. Cui, *Electrochim. Acta*, 2015, **163**, 330–337.

4 C. T. Wu, W. P. Liao and J. J. Wu, *J. Mater. Chem.*, 2011, **21**, 2871–2876.

5 A. S. Teja, A. Srivastava, J. A. K. Satrughna, M. K. Tiwari, A. Kanwade, S. C. Yadav and P. M. Shirage, *Dyes and Pigments*, 2022, 110997.

6 C.-P. Lee, C.-T. Li and K.-C. Ho, *Mater. Today*, 2017, **20**, 267–283.

7 S. C. Yadav, A. Srivastava, V. Manjunath, A. Kanwade, R. S. Devan and P. M. Shirage, *Mater. Today Phys.*, 2022, 100731.

8 A. Kanwade, S. Gupta, A. Kankane, A. Srivastava, S. C. Yadav and P. M. Shirage, *Sustainable Energy Fuels*, 2022, **6**, 3114–3147.

9 L. Song, P. Du, J. Xiong, F. Ko and C. Cui, *Electrochim. Acta*, 2015, **163**, 330–337.

10 S. C. Yadav, V. Manjunath, A. Srivastava, R. S. Devan and P. M. Shirage, *Opt. Mater.*, 2022, **132**, 112676.

11 X. Feng, K. Shankar, O. K. Varghese, M. Paulose, T. J. Latempa and C. A. Grimes, *Nano Lett.*, 2008, **8**, 3781–3786.

12 B. Liu and E. S. Aydil, *J. Am. Chem. Soc.*, 2009, **131**, 3985–3990.

13 Q. Kang, J. Cao, Y. Zhang, L. Liu, H. Xu and J. Ye, *J. Mater. Chem. A*, 2013, **1**, 5766–5775.

14 Y. Zhang, X. Xiong, Y. Han, X. Zhang, F. Shen, S. Deng, H. Xiao, X. Yang, G. Yang and H. Peng, *Chemosphere*, 2012, **88**, 145–154.

15 D. Zhang, F. Zeng and J. Russ, *J. Phys. Chem. A*, 2011, **85**, 1077–1083.

16 A. Kanwade, S. Gupta, A. Kankane, M. K. Tiwari, A. Srivastava, J. A. K. Satrughna, S. C. Yadav and P. M. Shirage, *RSC Adv.*, 2022, **12**, 23284–23310.

17 M. K. Tiwari, S. C. Yadav, A. Srivastava, A. Kanwade, J. A. K. Satrughna, S. S. Mali, J. V. Patil, C. K. Hong and P. M. Shirage, *RSC Adv.*, 2022, **12**, 32249–32261.

18 C. M. Teh and A. R. Mohamed, *J. Alloys Compd.*, 2011, **509**, 1648–1660.

19 S. Kment, H. K. Mentova, P. Kluson, J. Krysa, Z. Hubicka, V. Cirkva, I. Gregora, O. Solcova and L. Jastrabik, *J. Colloid Interface Sci.*, 2010, **348**, 198–205.

20 A. D. Paola, E. Garcia-Lopez, S. Ikeda, G. Marc, B. Ohtani and L. Palmisano, *Catal. Today*, 2002, **75**, 87–93.

21 M. Asilturk, F. Sayılkan and E. Arpac, *J. Photochem. Photobiol., A*, 2009, **203**, 64–71.

22 M. Litter and J. Navio, *J. Photochem. Photobiol., A*, 1996, **98**, 171–181.

23 B. Wang, Q. B. Li, W. Wang, Y. Li and J. Zhai, *Appl. Surf. Sci.*, 2011, **257**, 3473–3479.

24 A. Zaleska, *Recent Pat. Eng.*, 2008, **2**, 157–164.

25 N. A. Ökte and Ş. Akalın, *React. Kinet., Mech. Catal.*, 2010, **100**, 55–70.

26 Y. Hu, Y. Pan, Z. Wang, T. Lin, Y. Gao, B. Luo, H. Hu, F. Fan, G. Liu and L. Wang, *Nat. Commun.*, 2020, **11**, 1–10.

27 Y. Kim, S. Yang, E. H. Jeon, J. Baik, N. Kim, H. S. Kim and H. Lee, *Nanoscale Res. Lett.*, 2016, **11**, 1–8.

28 S. George, S. Pokhrel, Z. Ji, B. L. Henderson, T. Xia, L. J. Li, J. I. Zink, A. E. Nel and L. Mädler, *J. Am. Chem. Soc.*, 2011, **133**, 11270–11278.

29 W. Li, A. Kuc, C. F. J. Walther and T. Heine, *J. Phys. Chem. A*, 2015, **119**, 5742–5748.

30 Y. Wang, R. Zhang, J. Li, L. Li and S. Lin, *Nanoscale Res. Lett.*, 2014, **9**, 1–8.

31 T. Rawling, F. Buchholz and A. M. McDonagh, *Aust. J. Chem.*, 2008, **61**, 405–408.

32 S. Zhang, J. Jin, D. Li, Z. Fu, S. Gao, S. Cheng, X. Yu and Y. Xiong, *RSC Adv.*, 2019, **9**, 22092–22100.

33 J.-M. Ji, H. Zhou, Y. K. Eom, C. H. Kim and H. K. Kim, *Adv. Energy Mater.*, 2020, **10**, 2000124.

34 M. Thelakkat, C. Schmitz and H. W. Schmidt, *Adv. Mater.*, 2002, **14**, 577–581.

35 S. Ito, P. Liska, P. Comte, R. Charvet, P. Pechy, U. Bach, L. S. Mende, A. K. Zakeeruddin, M. K. Nazeeruddin and M. Grätzel, *Chem. Commun.*, 2005, 4351–4353.

36 B. Peng, G. Jungmann, C. Jager, D. Haarer, H. W. Schmidt and M. Thelakkat, *Coord. Chem. Rev.*, 2004, **248**, 1479–1489.

37 W. Y. Gan, S. W. Lam, K. Chiang, R. Amal, H. Zhao and M. P. Brungs, *J. Mater. Chem.*, 2017, **17**, 952–954.

38 M.-E. Ragoussi and T. Torres, *Chem. Commun.*, 2015, **51**, 3957–3972.

39 N. Sekar and V. Y. Gehlot, *Resonance*, 2010, **15**, 819–831.

40 T. Horiuchi, H. Miura, K. Sumioka and S. Uchida, *J. Am. Chem. Soc.*, 2004, **126**, 12218–12219.

41 F. Bella, N. V. lachopoulos, K. Nonomura, S. M. Zakeeruddin, M. Gratzel, C. Gerbaldi and A. Hagfeldt, *Chem. Commun.*, 2015, **51**, 16308–16311.

42 D. Ganta, J. Jara and R. Villanueva, *Chem. Phys. Lett.*, 2017, **679**, 97–101.

43 H. Zhou, L. Wu, Y. Gao and T. Ma, *J. Photochem. Photobiol., A*, 2011, **219**, 188–194.

44 F. Kabir, M. M. H. Bhuiyan, M. S. Manir, M. S. Rahaman and M. A. Khan, *Results Phys.*, 2019, **14**, 102474.

45 T. Jalali, P. Arkian, M. Golshan, M. Jalali and S. Osfouri, *Opt. Mater.*, 2020, **110**, 110441.

46 L. Xu, C. Aumaitre, Y. Kervella, G. Lapertot, C. Rodríguez-Seco, E. Palomares and P. Reiss, *Adv. Funct. Mater.*, 2018, **28**, 1706291.

47 N. S. Allen, N. Mahdjoub, V. Vishnyakov, P. J. Kelly and R. J. Kriek, *Polym. Degrad. Stab.*, 2018, **150**, 31–36.

48 M. Ismael, *J. Environ. Chem. Eng.*, 2020, **8**, 103676.

49 M. A. Khan, S. I. Woo and O. B. Yang, *Int. J. Hydrogen Energy*, 2008, **33**, 5345–5351.

50 B. Santara, P. K. Giri, S. Dhara, K. Imakita and M. Fujii, *J. Phys. D: Appl. Phys.*, 2014, **47**, 235304.

51 A. Pottier, C. Chaneac, E. Tronc, L. Mazerollesb and J.-P. Jolivet, *J. Mater. Chem.*, 2001, **11**, 1116–1121.

52 A. I. Hochbaum and P. Yang, *Chem. Rev.*, 2010, **110**, 527–546.

53 M. Law, L. E. Greene, J. C. Johnson, R. Saykally and P. Yang, *Nat. Mater.*, 2005, **4**, 455–459.

54 S. Li, Y. Wang, C. Gao, S. Ge, J. Yu and M. Yan, *J. Electroanal. Chem.*, 2015, **759**, 38–45.

55 P. Soundarrajan, K. Sankarasubramanian, T. Logu, K. Sethuraman and K. Ramamurthi, *Mater. Lett.*, 2014, **116**, 191–194.

56 Z. Weirong, Li Yajun, Z. Meng, Ch Jinsheng, X. Lihong, Sh Qiaomeng and Z. Xi, *Chem. Eng. J.*, 2016, **283**, 105–113.

57 A. P. Singh, S. Kumari, R. Shrivastav, S. Dass and V. R. Satsangi, *Int. J. Hydrogen Energy*, 2008, **33**, 5363–5368.

58 D. Devadiga and T. N. Ahipa, *Chem. Technol. Nat. Synth. Dyes Pigm.*, 2020, **5772**, 88939.

59 K. Hitoshi, H. Orita and H. Sugihara, *Langmuir*, 2008, **24**, 4411–4419.

60 A. I. Hochbaum and P. Yang, *Chem. Rev.*, 2010, **110**, 527–546.

61 A. Srivastava, B. S. Chauhan, S. C. Yadav, M. K. Tiwari, J. A. K. Satrughna, A. Kanwade, K. Bala and P. M. Shirage, *Chem. Phys. Lett.*, 2022, **807**, 140087.

62 M. Asiltürk, F. Sayılkan and E. Arpaç, *J. Photochem. Photobiol., A*, 2009, **203**, 64–71.

63 L. Long, L. Wu, X. Yang and X. Li, *J. Mater. Sci. Technol.*, 2014, **30**, 765–769.

64 D. Sinha, D. De, D. Goswami and A. Ayaz, *Mater. Today: Proc.*, 2018, **5**, 2056–2063.

65 H. Bashar, M. M. H. Bhuiyan, M. R. Hossain, F. Kabir, M. S. Rahaman, M. S. Manir and T. Ikegami, *Optik*, 2019, **185**, 620–625.

66 G. Salinas, M. José and M. J. Ariza, *Appl. Sci.*, 2019, **9**, 2515.

67 A. R. Samanchandra, D. Tharanga and G. A. Sewvandi, *Moratuwa Eng. Res. Con.*, 2017, 390–394.

68 H. Martínez, A. Ramon, M. Estévez, S. Vargas and R. Rodriguez, *Int. J. Mol. Sci.*, 2013, **14**, 4081–4093.

69 M. A. Almutairi, W. A. Farooq and M. S. AlSalhi, *Curr. Appl. Phys.*, 2021, **40**, 119–125.

70 S. Sathyajothi, R. Jayavel and A. C. Dhanemozhi, *Mater. Today: Proc.*, 2017, **4**, 668–676.

71 C. Pathak, K. Surana, V. K. Shukla and P. K. Singh, *Mater. Today: Proc.*, 2019, 665–670.